Center for Turbulence Research
Proceedings of the Summer Program 2010

Modeling of generation, propagation, and scattering of acoustic waves in the turbulent convection zone of the Sun

By K. V. Parchevsky AND A. G. Kosovichev†

We developed a three dimensional linear code for simulations of MHD waves in a gravitationally stratified medium with strong gradients of pressure and density in the presence of non-uniform background magnetic field and background flows. The code is suitable for analysis of excitation, propagation, and transformation of MHD waves in realistic models of sunspots. Such a code can be used for producing artificial data for testing and calibration of heliosesmic inversion techniques used for analysis of data from the space missions SOHO/MDI, HINODE, and SDO/HMI.

Comparison of a travel time difference map obtained from simulated artificial data by the standard time-distance techniques shows good agreement with the theoretical prediction calculated in the ray-path approximation. This verifies the consistency and accuracy of time-distance techniques used in the reconstruction of subphotospheric flows. Simulations of MHD waves in a realistic sunspot model calculated by M. Rempel using a non-linear MHD code show the existence of the strong mixture of slow and Alfven waves near the source location (e.g. the magnetostatic background model) and skewness of the wave front of the fast MHD wave (e.g. pure acoustics with background flows).

1. Introduction

Understanding of acoustics wave generation, propagation, and scattering in the convective zone of the Sun is one of the high-priority tasks of helioseismology. Acoustic waves in the Sun are generated by a turbulent convection. Doppler measurements of the photospheric line-of-sight oscillation velocities provide information about the acoustic wave field, which can be used for reconstruction of the internal structure of the Sun (sound speed profile) and its dynamics (background flows) using helioseismic inversion techniques. Such observations are provided by the SOHO, Hinode, and SDO space missions. Acoustic ray theory tells us that solar acoustic waves propagate in the convective zone along curved paths between top and bottom turning points, but in reality the situation is much more complicated. Acoustic ray theory is not applicable near the top turning point (near the photosphere) where the background model changes quickly due to large gradients of pressure and density, and wave effects must be taken into account. Actual wave field is a mixture of acoustic and surface gravity waves. Not all waves are reflected by the photosphere. Waves with frequencies higher than the acoustic cut-off frequency are not reflected by the photospheric acoustic potential barrier but instead propagate to the chromosphere and higher. Even modes with frequencies lower than the acoustic cut-off frequency can leak through this barrier causing additional damping. Waves can be scattered by the inhomogeneities of the solar structure: sunspots and background flows. Taking the magnetic field into account further complicates the situation. Now

† HEPL, Stanford University, Stanford, CA 94305, USA

waves, purely acoustic before they enter a magnetic region (sunspot, active region), can be converted into different types of MHD waves: fast, slow, and Alfven waves. Numerical simulations are important for understanding the behavior of the acoustic waves in the complicated solar environment and provide the artificial data for calibration of helioseismic inversion techniques used for processing data from space missions SOHO, Hinode, and SDO.

2. Preliminaries

2.1. *Formulation*

Propagation of waves inside the Sun, in the presence of magnetic fields and velocities in the background state, is described by the following system of linearized MHD equations:

$$\begin{aligned}
\frac{\partial \rho}{\partial t} &= -\nabla\cdot\boldsymbol{m}' - \nabla\cdot(\rho'\boldsymbol{V}_0)\\
\frac{\partial \boldsymbol{m}'}{\partial t} &= -\nabla p' - (\boldsymbol{m}'\cdot\nabla)\boldsymbol{V}_0 - (\boldsymbol{V}_0\cdot\nabla)\boldsymbol{m}' - \boldsymbol{m}'\nabla\cdot\boldsymbol{V}_0 - \rho'(\boldsymbol{V}_0\cdot\nabla)\boldsymbol{V}_0\\
&\quad -\frac{1}{4\pi}\nabla(\boldsymbol{B}_0\cdot\boldsymbol{B}') + \frac{1}{4\pi}[(\boldsymbol{B}_0\cdot\nabla)\boldsymbol{B}' + (\boldsymbol{B}'\cdot\nabla)\boldsymbol{B}_0] + \rho'\boldsymbol{g}_0 + \boldsymbol{S}(\boldsymbol{r},t)\\
\frac{\partial \boldsymbol{B}'}{\partial t} &= \nabla\times\left(\frac{\boldsymbol{m}'}{\rho_0}\times\boldsymbol{B}_0\right) + \nabla\times(\boldsymbol{V}_0\times\boldsymbol{B}')\\
\frac{\partial p'}{\partial t} &= c_s^2\frac{\partial\rho}{\partial t} - c_s^2\boldsymbol{m}'\cdot\left(\frac{\nabla p_0}{\Gamma_1 p_0} - \frac{\nabla\rho_0}{\rho_0}\right) - c_s^2\rho_0\left(\frac{p'}{p_0} - \frac{\rho'}{\rho_0}\right)\nabla\cdot\boldsymbol{V}_0\\
&\quad -\boldsymbol{V}_0\cdot\nabla p' + c_s^2\boldsymbol{V}_0\cdot\nabla\rho',
\end{aligned} \tag{2.1}$$

where ρ', p', $\boldsymbol{m}' = \rho_0\boldsymbol{v}'$, and $\boldsymbol{B}'$ are the perturbations of the density, pressure, momentum, and magnetic field respectively. Quantities p_0, ρ_0, c_s, $\boldsymbol{g}_0$, $\boldsymbol{V}_0$, and $\boldsymbol{B}_0$ are the background pressure, density, sound speed, gravitational acceleration, flow velocity, and the magnetic field respectively. The forcing term $\boldsymbol{S} = (0, 0, S_z(\boldsymbol{r}, t))$ represents the source of z-component of force. The source is localized in space and explicitly depends on time as Rickers wavelet:

$$\begin{aligned}
S_z(\boldsymbol{r},t) &= AG(\boldsymbol{r})F(t),\\
G(\boldsymbol{r}) &= \left(1 - \frac{(z-z_{src})^2}{H_{src}^2}\right)^2\left(1 - \frac{(x-x_{src})^2 + (y-y_{src})^2}{R_{src}^2}\right)^2\\
F(t) &= \left(1-2\tau^2\right)e^{-\tau^2},\quad \tau = \frac{\omega_0(t-t_0)}{2} - \pi,\quad t_0 \le t \le t_0 + \frac{4\pi}{\omega_0},
\end{aligned} \tag{2.2}$$

where x_{src}, y_{src}, and z_{src} are the coordinates of the source center; H_{src} and R_{src} are the vertical and horizontal sizes of the source, respectively; ω_0 is the central source frequency; t_0 is the moment of the source initiation. In our simulations we chose $H_{src} = 0.1$ Mm, $R_{src} = 0.3$ Mm, and $\omega_0 = 3.5$ mHz. This source model provides the wave spectrum, which closely resembles the solar spectrum. It has a peak near the central frequency ω_0 and spreads over a broad frequency interval. The source spectrum is

$$|\hat{F}(\omega)| \equiv \left|\int_{-\infty}^{\infty} F(t)e^{-i\omega t}\,\mathrm{d}t\right| = 4\sqrt{\pi}\,\frac{\omega^2}{\omega_0^3}\,e^{-\frac{\omega^2}{\omega_0^2}} \quad . \tag{2.3}$$

A superposition of such sources with uniform distribution of central frequencies randomly distributed below the photosphere describes very well the observed solar oscillation spectrum (see details in Parchevsky & Kosovichev 2007).

2.2. *Numerical Scheme and Boundary Conditions*

We used a semi-discrete numerical scheme. In this approach the space and time discretization processes are separated. First the spatial discretization using a uniform grid is performed, leaving the problem continuous in time. The spatial derivatives are approximated by the finite-difference (FD) scheme using a symmetrical stencil. Such approach enables the combination of different versions of spatial discretization and time advancing schemes. Usually, dispersion-relation-preserving scheme of the 4th-order (Tam & Webb 1993) is used for spatial discretization, which minimizes the Fourier transform error of the numerical scheme and preserves the dispersion relation of the continuous problem in discrete formulation for shorter wavelength than the classic FD scheme. Strong stability preserving the Runge-Kutta scheme (Shu 2002) is used for time advancing. Waves with the wavelength less than $4\Delta x$ are not resolved by the FD scheme. They lead to point-to-point oscillations of the solution that can cause a numerical instability. Such waves have to be filtered out. We used a 6th-order digital filter to eliminate unresolved short wave components from the solution.

The theoretical accuracy of high-order FD schemes can be reached only if they are combined with adequate numerical boundary conditions. It is easy to derive non-symmetric boundary operators that approximate the first derivative near boundaries with high order. However, such approximations are often unstable. We follow Carpenter 1993 and use an implicit Padé approximation of the spatial derivatives in z-direction near the top and bottom boundaries to derive stable 3rd-order boundary conditions compatible with the numerical scheme for internal points of the domain.

In addition to maintaining numerical and convective stabilities we have to prevent spurious reflections of acoustic waves from the boundaries. In this paper, we follow Hu 1996, who proposed a Perfectly Matched Layer (PML) procedure for Euler equations. The waves with frequencies lower than acoustic cut-off frequency are reflected below the photosphere. The waves with higher frequencies pass through and go to the chromosphere. To simulate such frequency-dependent reflecting property we put the PML at 500 km above the photosphere. On the Sun all waves that reach this layer propagate farther to the chromosphere. In simulations they will be absorbed by the PML and do not pollute the computational domain. To prevent spurious reflection from the bottom of the domain we put the PML at the bottom boundary. The lateral boundary conditions are chosen to be periodic, which preserves balance of the incoming and outgoing waves, important for helioseismic analysis.

3. Results and Discussion

3.1. *Background flows*

One of the main goals of helioseismology is to reconstruct the internal structure (sound speed, magnetic field, velocity field) of active regions on the Sun from observation of solar oscillations. For improving the helioseismic techniques (taking into account wave effects) we need numerical simulations for better understanding of the details of excitation, propagation, and scattering of MHD waves in magnetized turbulent regions. These simulations also provide artificial data for testing and calibrating helioseismic inversion

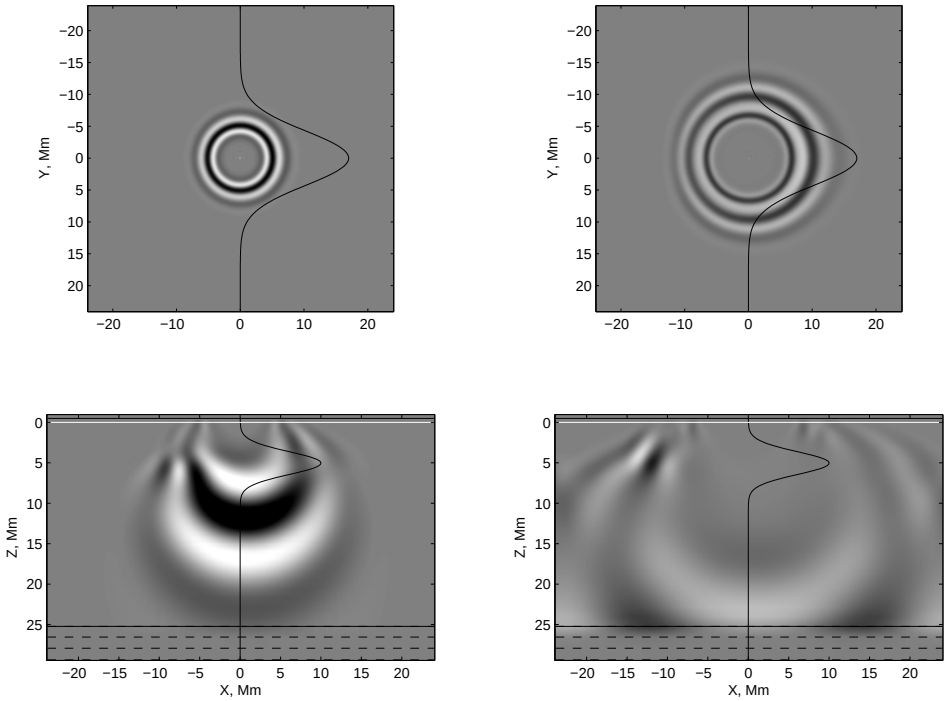

FIGURE 1. Snapshots of the wave field generated by a single source in the presence of the background x-jet flow. The left panels represent horizontal (top) and vertical (bottom) slices at the moment $t = 16.7$ min., the right panels show the same slices at $t = 22.5$ min. The thin solid black line in both panels indicates the velocity profile of the x-jet. The maximum jet velocity is 5 km/s.

methods. As an initial step we study the interaction of seismic waves with magnetic and flow fields separately.

We chose the standard solar model S by Christensen-Dalsgaard 1996 with a superimposed x-jet flow field as a background state (without magnetic field). The jet has Gaussian vertical and horizontal profiles. The depth of the jet is 5 Mm. The size of the domain is $48\times48\times30$ Mm^3 ($320\times320\times88$ nodes). Figure 1 shows snapshots of the wave front generated by a single source at different moments of time. The source is located at the depth of 100 km below the photosphere. The top panels show horizontal slices of the domain at the level of the photosphere. The white horizontal lines in the bottom panels show the position of the photosphere. The bottom panels show vertical slices of the domain. The vertical profile of the wavefront at $t = 16.7$ min (left panels) is noticeably skewed when the horizontal profile remains circular. Acoustic waves that form the wavefront at the photospheric level at this moment of time do not propagate deeply enough and do not reach the jet. At later moments of time the photospheric wavefront is skewed because it is formed by waves that propagate through deeper layers and reach the jet.

To check the accuracy of the helioseismic method of travel-time determination we simulated the wave field from multiple sources given by Eq. (2.2), randomly distributed at a depth of 100 km below the photosphere.

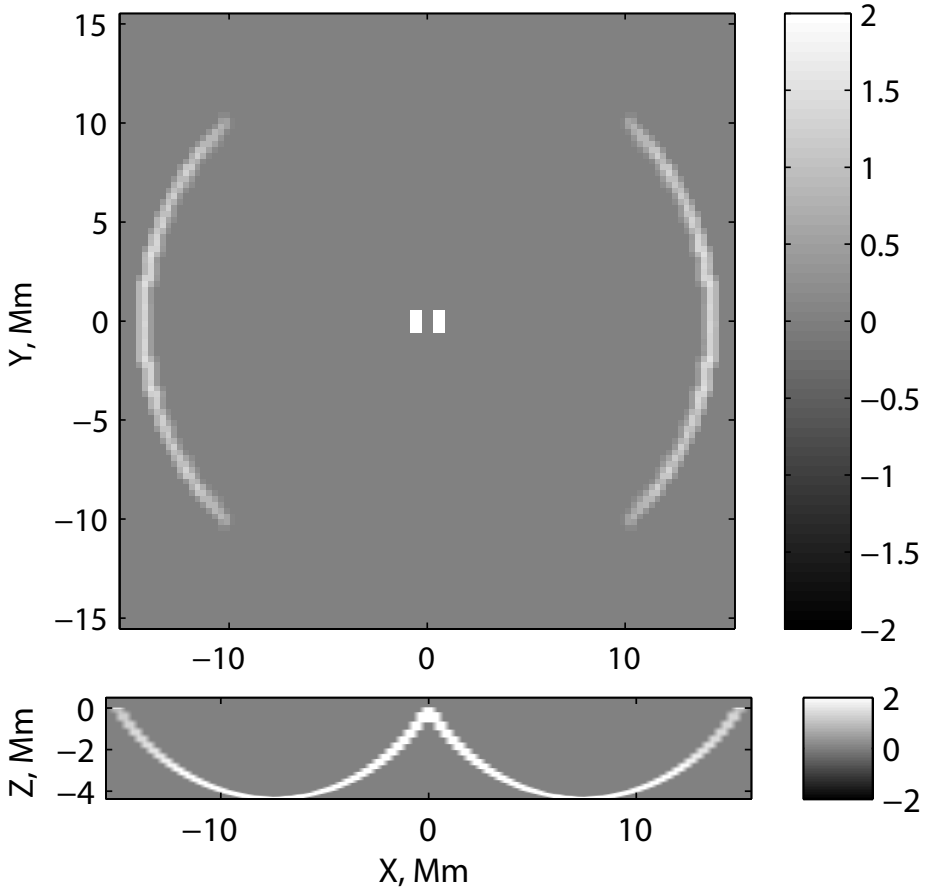

FIGURE 2. Three-dimensional east-west x-component of the flow kernel, calculated in the ray-path approximation for the annulus with radius of 15 Mm and width of 1 Mm in s/Mm^3.

The relationship between the travel time difference and the background velocity field in ray-path approximation is given by an integral equation

$$\delta\tau_{diff} = -2\int_{\Gamma} \frac{\boldsymbol{n}\cdot\boldsymbol{V}}{c_s^2}\,\mathrm{d}s = -2\int_{\Gamma} \frac{\boldsymbol{n}}{c_s}\cdot\boldsymbol{K}_f\,\mathrm{d}s, \tag{3.1}$$

where the second equality sign can be considered as a definition of the flow kernel $\boldsymbol{K}_f$. The three-dimensional east-west x-component of the flow sensitivity kernel calculated in the ray-path approximation is shown in Fig. 2. The top panel represents the horizontal slice of the three-dimensional kernel K_x near the photospheric level. The bottom panel shows the vertical cut of the flow sensitivity kernel. The gray scale is given in units s/Mm^3. The travel-time map, calculated from the simulated wave field for the same annulus, is shown in the left panel of Fig. 3. Travel times were obtained by the standard helioseismic procedure (fitting the cross-correlation function by the Gabor's wavelet). The solid curve in the right panel represents the horizontal average of the travel-time difference map. The dashed curve shows the theoretical travel-time difference profile calculated in the ray-path approximation using equation (3.1) and the three-dimensional sensitivity kernel from Fig. 2. We see very good agreement between theoretical and observational (calculated from

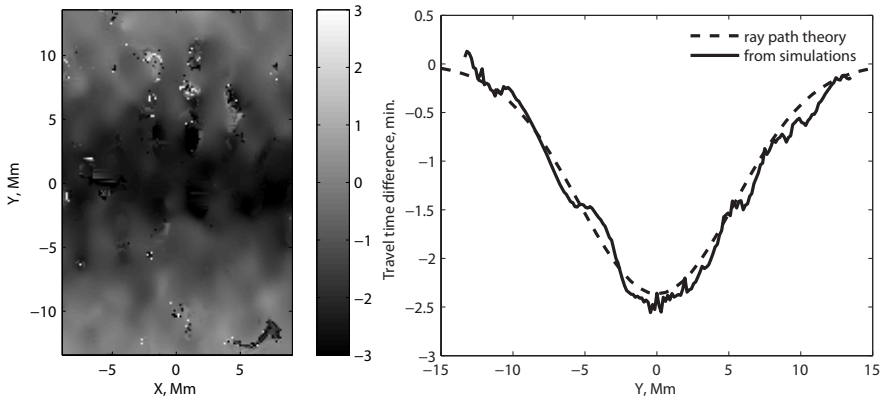

FIGURE 3. Travel time difference map (in minutes) obtained from artificial simulated wave field by the standard helioseismic procedure (left). The solid curve in the right panel shows the horizontal average of the travel time difference map. The dashed curve represents the theoretical travel time difference profile calculated in the ray-path approximation.

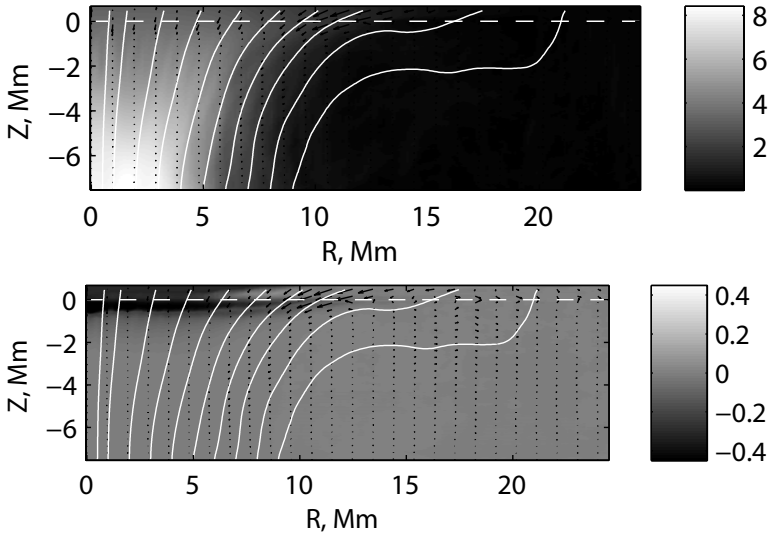

FIGURE 4. Axially symmetric model of the sunspot obtained by the angular averaging of the realistic sunspot model calculated by M. Rempel. The top panel represents the strength of the magnetic field (kG), the bottom panel shows relative perturbation of the sound speed $\delta c/c$. The white curves in both panels show magnetic field lines. Maximum speed of the flow is about 2.3 km/s

artificial data) profiles of the travel-time difference, which confirms the consistency and accuracy of the time-distance helioseismic techniques.

3.2. *MHD Wave Propagation in Realistic Sunspot Model*

In this section we present results of the numerical simulations of MHD wave propagation in the realistic model of the sunspot with the background flows. The background sunspot model, shown in Fig. 4, represents an angular averaged snapshot of a three-dimensional sunspot model calculated by Rempel 2009 using non-linear MHD simulations. The gray scale in the top panel shows the strength of the magnetic field in kG, and the gray scale

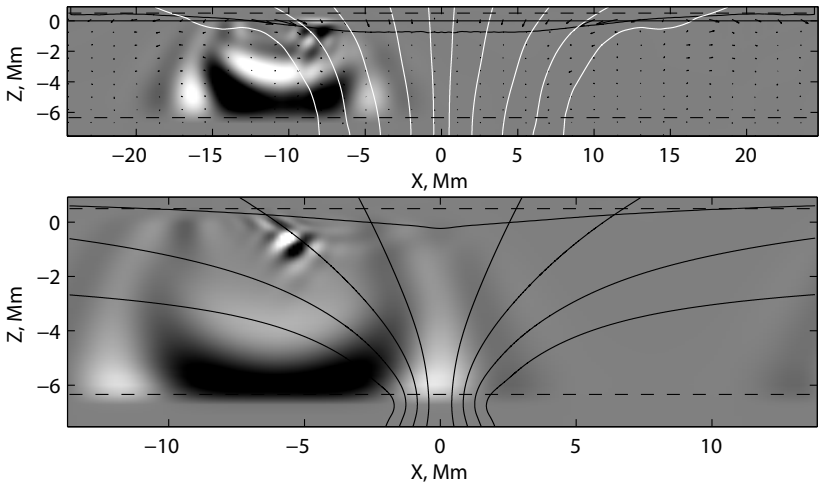

FIGURE 5. Snapshot of the vertical slice of the z-component of momentum $\rho_0 w'$ at the moment $t = 13.3$ min. The top panel shows wave simulations in Rempel's realistic model of the sunspot. For comparison, we also show simulations of MHD waves in the magnetostatic sunspot model (bottom). In both cases we see strong mixture of slow and Alfven waves near the origin of the wave source. The wave front in the magnetostatic (no background flows) model remains symmetric, whereas in Rempel's sunspot model it is skewed by the background flows.

in the bottom panel shows relative perturbation of the sound speed $\delta c_s/c_s$. Horizontal relative variations of the sound speed are negligible in regions deeper than 1.5 Mm. The white dashed line near the top boundary of both panels marks the position of the photosphere. Arrows show the direction and speed of the background flow (maximum value is about 2.3 km/s).

Simulations of MHD waves generated by a single source in the realistic sunspot model are shown in the top panel of Fig. 5. For comparison, in the bottom panel we present simulations of MHD waves from the same source in the magnetostatic (Pizzo 1986) sunspot model. The black solid curves near the top boundary of both panels represent the level of $\beta = 1$, where $\beta = p_g/p_m$ is the ratio of the gas and magnetic pressure.

The two simulations have both common features and differences. In both simulations a strong mixture of slow MHD and Alfven waves is generated near the source location. These waves slowly propagate along the magnetic field lines. The shape of the wave front of the fast MHD wave in the magnetostatic model remains symmetric, whereas in simulations with a realistic model of the sunspot it is noticeably skewed by the background flows, similar to that shown in Fig. 1.

We have shown here preliminary results of MHD wave simulations in the realistic sunspot model with background flows. Future plans are to calculate wave fields from randomly distributed wave sources and use them as artificial data for testing helioseismic inversion techniques.

4. Conclusions

We developed a three-dimensional linear code for simulation of excitation, propagation, scattering, and transformation of MHD waves in a gravitationally stratified medium in presence of the sharp gradients of background pressure, density, non-uniform background

magnetic field, and flows, which makes this code suitable for studying propagation of MHD waves in realistic models of sunspots.

We used a non-magnetic version of the code to generate artificial helioseismic data from randomly distributed wave sources in presence of a simple jet-like background flow located at the depth of 5 Mm below the photosphere (the standard solar model S was chosen as a background model). Using the standard time-distance technique we calculated the travel time difference map from these artificial data. Comparison of the travel time difference profile with the theoretical prediction based on the ray-path theory of solar oscillations shows very good agreement.

We performed preliminary simulations of MHD waves in the realistic model of the sunspot with the background flows. Results of simulations show characteristic features of both cases: magnetostatic background model (no flows) and pure acoustic (no magnetic filed) with the background flow.

Future plans are to calculate a wave field from multiple sources in the realistic background model of a sunspot and produce artificial helioseismic data for testing and calibration of helioseismic techniques used for analysis of data obtained from space missions SOHO/MDI, HINODE, and SDO/HMI.

5. Acknowledgements

We are grateful to Matthias Rempel for providing us realistic simulations of the sunspot model with the background flows. We also grateful to Kaori Nagashima who calculated the travel time difference map from artificial helioseismic data.

REFERENCES

Parchevsky, K. V. & Kosovichev, A. G. 2007 Three-dimensional numerical simulations of the acoustic wave field in the upper convection zone of the Sun. *Astrophys. J.*, **666**, 547-558.

Tam, C. & Webb, J. 1993 Dispersion-relation-preserving finite difference schemes for computational acoustics. *J. Comput. Phys.*, **107**, 262-281.

Shu, C.-W. 2002 A survey of strong stability preserving high-order time discretizations in Collected lectures on the preservation of stability under discretization, eds. D. Estep and S. Tavener, *SIAM*, 51-65.

Carpenter, M.H., Gottlieb, D., and Abarbanel, S. 1993 The stability of numerical boundarytreatmentfor compact high-order finite-difference schemes. *J. Comput. Phys.*, **108**, 272-295.

Hu, F. Q. 1996 On absorbing boundary conditions for linearized Euler equations by a perfectly matched layer. *J. Comput. Phys.*, **129**, 201-219.

Christensen-Dalsgaard, J., et al. 1996 The current state of solar modeling. *Science*, **272**, 1286-1292.

Rempel, M., Schussler, M., Cameron, R.H., Knolker, M. 2009 Penumbral Structure and Outflows in Simulated Sunspots. *Science*, **325**, 171-174.

Pizzo, V.J. 1986 Numerical solution ofthe magnetostatic equations for thick flux tubes, with application to sunspots, pores, and related structures. *Astrophys. J.*, **302**, 785-808.